Nanoscale

www.rsc.org/nanoscale

Volume 4 | Number 5 | 7 March 2012 | Pages 1387–1806

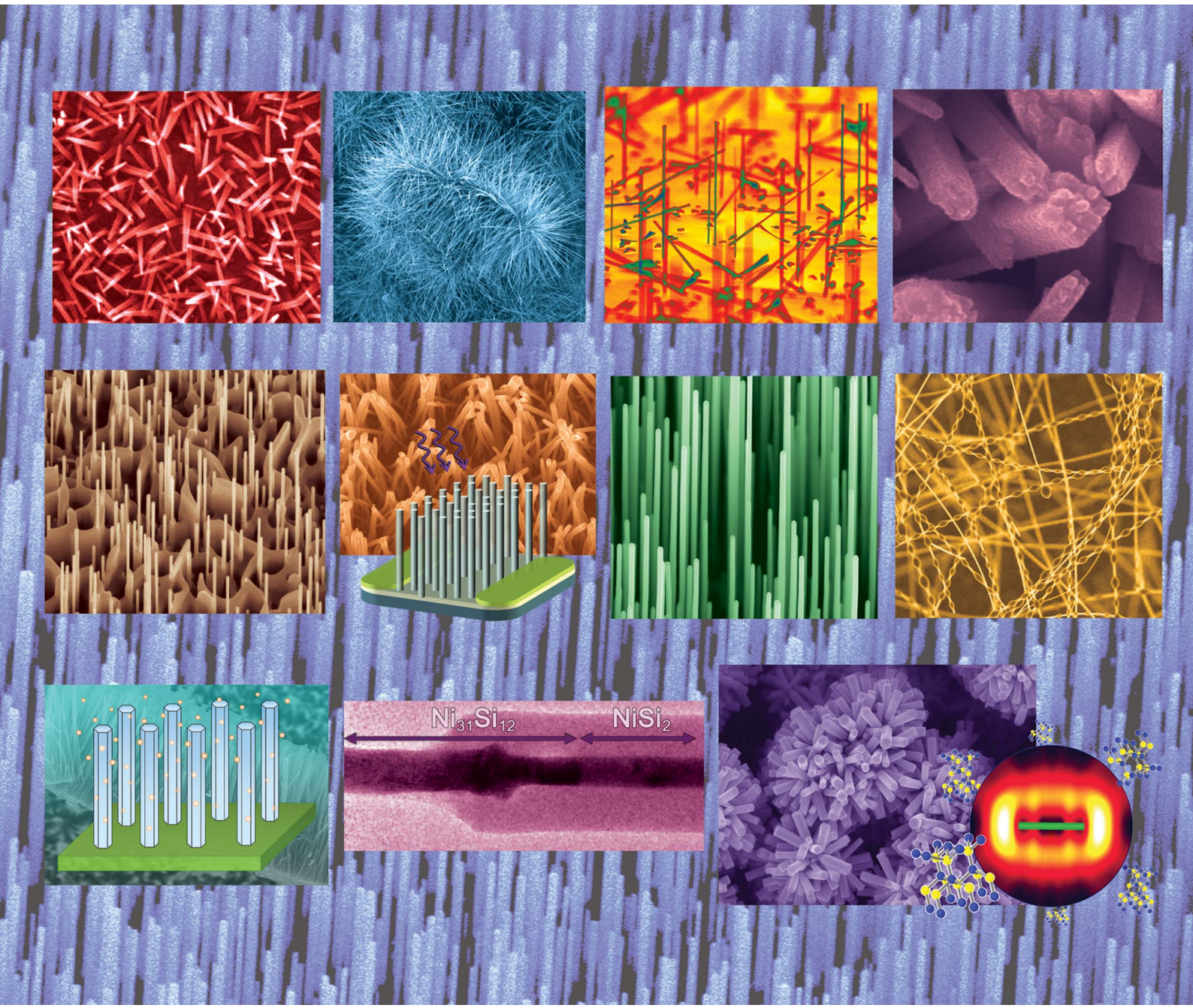

ISSN 2040-3364

RSC Publishing

NCNST

2040-3364(2012)4:5;1-L

View Online / Journal Homepage / Table of Contents for this issue
Dynamic Article Links

Nanoscale

Cite this: *Nanoscale*, 2012, **4**, 1446

www.rsc.org/nanoscale

FEATURE ARTICLE

Anisotropic photonic properties of III–V nanowires in the zinc-blende and wurtzite phase†

Christophe Wilhelm,[ab] Alexandre Larrue,[b] Xing Dai,[c] Dmitri Migas[d] and Cesare Soci*[abc]

Received 6th January 2012, Accepted 3rd February 2012
DOI: 10.1039/c2nr00045h

Some critical aspects of the anisotropic absorption and emission properties of quasi one-dimensional structures are reviewed in the context of III–V compound semiconductor nanowires. The unique optical and electronic properties of III–V nanowires stem from the combination of dielectric effects due to their large aspect ratio, and their specific crystallographic structure which can differ significantly from the bulk case. The growth conditions leading to single-crystal nanowires with either zinc blende or wurtzite phase are first presented. Dipole selection rules for interband transitions in common III–V compounds are then summarized for the two different phases, and corroborated by *ab initio* Density Functional Theory calculations of the oscillator strength. The optical anisotropy is discussed considering both the effect of refractive index mismatch between the nanowire and its surroundings and the polarization of the emitting dipoles set by the nanowire crystallographic structure and orientation. Finite Difference Time Domain simulations are finally employed to illustrate the influence of the emitting dipole orientation and the nanowire diameter on the distribution of radiation in the far-field. The importance of the correlation between structural and optoelectronic properties is highlighted in view of potential applications in future nanowire photonics.

1. Introduction

Semiconductor nanowires are promising components for the development of innovative functional systems where large sensitivity,[1] dense integration,[2–5] and complex polymorphic heterostructures[6–9] are desired. Thanks to their direct bandgap, versatility in bandgap engineering, and high electron mobility,[10,11] III–V compound semiconductor nanowires are the most suitable choice for optoelectronic applications. Following the tremendous improvement in controlled bottom-up synthesis,[12] the interest in III–V nanowire photonic properties for 3D on-chip integration of compact light sources,[13] optical switches and interconnects is rising quickly.[14–16]

Nanowire light absorption and emission properties are strongly influenced not only by the electronic properties of the constituent materials, but also by the dielectric contrast with the surrounding enhanced by their large aspect ratio and, in the sub-wavelength regime, by unconventional mechanisms of light-matter interaction and light propagation. Furthermore, for sufficiently small radial dimensions or when comprising of heterostructures on the atomic length scale, nanowires display characteristic quantum behaviors of low-dimensional structures, which further enriches the fundamentals of their photonic behavior.[17] It is noteworthy that all these aspects are inherently anisotropic, hence the emergence of future nanowire applications in optoelectronics will rely on a deeper understanding of their interplay in determining the overall spatial and polarization anisotropy of light absorption and emission.

Recent advances in understanding bottom-up III–V nanowire synthesis have enabled mastering the growth parameters that determine the crystalline structure and the demonstration of complex functional architectures, opening up a whole new range of possibilities in engineering and investigating nanowire-based photonic elements and their optical anisotropy. The aim of this article is to identify various sources of anisotropy and their physical origin in optically active III–V nanowires based on some of the relevant works appeared in the recent literature. Original contributions to evaluate the dipole selection rules in common III–V materials as well as diameter-dependent far-field radiation patterns are also presented with the intent of providing a complete reference workflow for the analysis of the absorption and emission properties of specific nanowires. As nanowire technology progresses rapidly, the comprehensive analysis of *intrinsic* (*i.e.* electronic) and *extrinsic* (*i.e.* dielectric) factors

[a]*Division of Microelectronics, School of Electrical and Electronic Engineering, Nanyang Technological University, 50 Nanyang Avenue, Singapore 639798. E-mail: csoci@ntu.edu.sg*
[b]*CINTRA CNRS-NTU-Thales, UMI 3288, Research Techno Plaza, 50 Nanyang Drive, Singapore 637553*
[c]*Division of Physics and Applied Physics, School of Physical and Mathematical Sciences, Nanyang Technological University, 21 Nanyang Link, Singapore 637371*
[d]*Belarusian State University of Informatics and Radioelectronics, 6 Browka str, 220013 Minsk, Belarus*
† This article was submitted as part of a collection highlighting papers on the 'Recent Advances in Semiconductor Nanowires Research' from ICMAT 2011.

affecting their photonic properties is becoming crucial to account for theoretical predictions in actual experiments.

The paper is organized in three sections: Section 2 summarizes the crystalline properties of III–V nanowires grown by common bottom-up methodologies and the correlation between crystalline phase (*i.e.* zinc blende or wurtzite) and growth parameters. The bulk optical properties (*i.e.* the origin of the lowest optical transitions and dipole selection rules) of common III–V materials in the zinc blende or wurtzite phase are presented in Section 3. The optical anisotropy of III–V nanowires is finally considered in Section 4, where the effects of refractive index mismatch and crystalline structure on the spatial (*i.e.* radiation pattern in the far-field) and the polarization anisotropy of the emission are presented for specific III–V nanowire materials and structures.

2. III–V nanowire growth and crystal structure

While bulk III–V materials usually crystallize in the zinc blende (ZB) cubic structure, with the exception of ionic III-nitride compounds which normally exhibit wurtzite (WZ) hexagonal structure, III–V nanowires commonly display ZB and WZ polymorphism.[9,12,18–20] Fig. 1a and 1b show the atomic arrangement of ZB and WZ structures along the <111> and <0001> nanowire growth directions: while the ZB structure results from the stacking of monoatomic layers in the sequence of …cAaBbCcA… in the <111> direction, the WZ structure shows a stacking sequence of the kind …bAaBbA… in the <0001> direction. Since the two structures are very similar, polymorphism is manifested by the appearance of small segments of ZB in WZ when a stacking fault misplaces an "Aa" plane with a "Cc" plane, or in the appearance of small WZ segments in ZB after the introduction of two sequential twin planes.[9,18,21] The fraction of these "faulty" segments within the primary phase is often regarded as the likelihood of nucleating seeds and growing single crystal nanowires in either of the two phases (Fig. 1c–1e).[9,22–25]

Bottom-up methods for the growth of III–V nanowires include Metal Organic Chemical Vapor Deposition (MOCVD),[26,27] Molecular Beam Epitaxy (MBE),[23] and Chemical Beam Epitaxy (CBE),[28] which commonly rely on the Vapor–Liquid–Solid (VLS) mechanism.[29] The VLS method is based on the formation of a supersaturated alloy inside a liquid seed nanoparticle (typically Au) from gaseous precursors. Nanowires grow in a layer-by-layer fashion atop the (111) low-energy surface, where nucleation is believed to occur at the vapor-liquid-solid interface.[30] Notably, both the supersaturation of the liquid nanoparticle and the interface energies at the triple phase boundary have strong influence on the nucleation process and the resulting crystallographic phase.[31] The appearance of a certain structure can therefore be controlled by tuning relevant VLS growth parameters such as temperature, V/III ratio, and radius. For a given material system and crystal orientation, the surface energy of WZ lateral facets is generally lower than those of ZB, favoring the appearance of WZ phase in small diameter nanowires where surface-to-volume ratio is high.[18,31–33] Moreover, the Gibbs–Thomson effect is also believed to affect the energetic of nanowires with small radii above the critical thickness and also favor the formation of WZ structure.[34–36] It is generally accepted that high supersaturation favors the appearance of a WZ crystalline phase.[31,35–37] Thus, growth

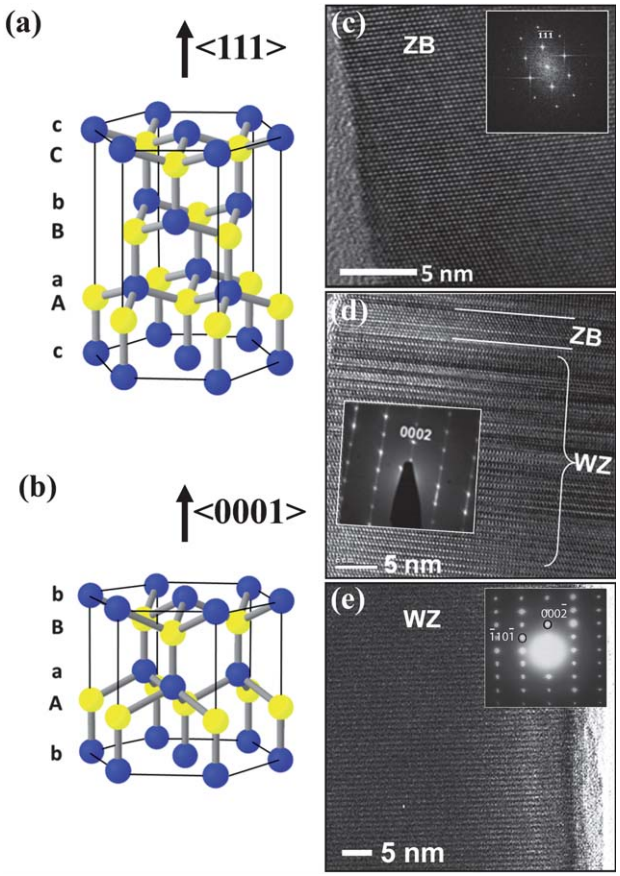

Fig. 1 Polymorphism in III–V nanowires. Ball-and-stick model of (a) the ZB structure in the <111> growth direction, showing the sequence of monoatomic stacking planes…cAaBbCc… and (b) the WZ structure in the <0001> growth direction with stacking plane sequence…bAaBb… (c–e) High resolution TEM images of: (c) GaAs nanowire grown on GaAs (111) B surface. The electron diffraction pattern in the inset shows a pure ZB phase.[45] (d) GaAs nanowire grown on Si (111) exhibiting a mixture of ZB and WZ phases. Reprinted from ref. 12, with the permission from Elsevier. (e) Stacking fault free GaAs nanowire displaying pure WZ phase. Reprinted with permission from ref. 46 (Copyright 2009, American Institute of Physics).

temperature is arguably the most effective parameter to control the nanowire crystallographic structure. For a given precursor molar fraction, supersaturation increases at higher temperatures promoting WZ;[18,27,36] however, temperature influences significantly the thermodynamic stability of sidewall facets (nanowire surface reconstruction), and may increase structural uncertainties and defects.[27] Precursor V/III ratio also affects supersaturation, together with surface and interfacial energies, which in turn affect the formation of twins at the triple phase contact line.[24] Consequently, structure can be tuned by different precursor molar fractions with a fixed V/III ratio[7,38] as well as varying the V/III ratio by changing group V or group III molar fractions independently.[23,24] Since the solubility of group V in the liquid seed particle is typically lower than group III, decreasing the V/III ratio will increase supersaturation and favor the WZ phase.[24] However, large group V molar fractions tend to decrease surface and interfacial energies, hence to favor the ZB phase. Large relative fractions of WZ are therefore obtained at

small V/III ratios and small group V molar flows. These trends have been generally observed for different material systems, including GaAs,[18,24,39] InAs[27] and InP[18,25,40] nanowires grown either homoepitaxially or heteroepitaxially on Si substrates.[41,42] It is also worth noting that similar growth conditions for the synthesis of pure WZ phase (*i.e.* high growth temperature, low V/III ratio and small radii) apply to the case of Selective Area (SA) nanowire growth, which does not rely on the use of metal seed particles.[22,43] For reference, some of the reported growth conditions leading to preferential crystallization in the ZB or WZ phase are reported in Table 1. Note that InAs seems to constitute an exception to this general trend, where the proportion of WZ phase was found to increase by decreasing growth temperature.[9,34]

The remarkable advances in controlling the crystallographic properties of III–V nanowires by the VLS mechanism have enabled the realization of axial periodic structures, such as polytypic superlattices made of alternating segments with different phases[9] or twinning superlattices based on the repetition of segments with constant length between twin planes. Such structures are extremely interesting for the engineering of unique optoelectronic properties by the introduction of crystallographic inhomogeneities in otherwise homogeneous materials. Quasi-periodic twinning superlattices have been first demonstrated in GaP and InP nanowires grown by pulsed laser assisted CVD growth.[8] The formation of twinning superlattices has been further investigated in the growth of InAs,[9] InP,[6] and GaP[7,44] nanowires by MOCVD, and quantitatively explained by a model based on two-dimensional nucleation and deformation of the liquid droplet during the VLS growth.[6,44] According to this model, twinning superlattices are naturally occurring at specific growth temperatures and nanowire diameters (the larger the diameter, the longer the spacing between twin planes).[9] Impurity dopants, such as Zn, have also been used to further decrease the activation barrier for two-dimensional nucleation growth of ZB and produce long-range ordered twinning superlattices in InP and GaP nanowires. In this case the spacing between twin planes was also proportional to the Zn doping concentration in addition to the nanowire diameter.[6,7]

3. Structural and optoelectronic properties of common III–V semiconductors

Since the optoelectronic properties of III–V crystals in the ZB and WZ phase are significantly different, the co-existence of both phases in nanowire systems raises the issue of distinguishing and identifying specific contributions from the two structures. On the other hand, the availability of two phases with distinct electronic and optical properties within the same material system, combined with the wide variety of III–V materials covering the entire spectral range from visible to medium infrared, offer unprecedented flexibility for bandgap engineering toward the design of novel light detection and emission systems. Theoretical calculations of the band structure of the most common III–V binary compounds (except for GaP) predict the persistence of the direct character of the energy gap situated at the Γ point when transitioning from the stable (primary) to the energetically unfavorable (secondary) structure. As a reference, literature values of direct bandgap energies of the two phases at room and low temperature are summarized in Table 2, and a schematic of the energy levels involved in the lowest energy optical transitions at the Γ point are depicted in Fig. 2. At the highly symmetric Γ point, each band has numerous possible symmetries for the wave-function. For convenience, here we adopt the so-called "BSW" notation that labels the combination of all possible symmetries for a given band with a single number (for example, in the case of ZB with no spin–orbit, the transition occurs between Γ_{1c} and Γ_{15v}, where 1 and 15 identify the symmetries, and *c* and *v* stand for conduction and valence band respectively).[47] Without spin–orbit interaction, the transition from ZB to WZ structure causes the valence band to split at the Γ point, with a crystal-field splitting denoted by Δ_{Cryst}. As a result, one transition (Γ_{1c}–Γ_{15v}) and two transitions (Γ_{1c}–Γ_{6v} and Γ_{1c}–Γ_{1v}) are generally possible in the case of ZB and WZ, respectively.

The symmetry of the crystalline structure manifests in the polarization of the dipole transitions by introducing anisotropy in optical properties such as the dielectric function or the absorption coefficient. These parameters are generally represented by a second order tensor, where the number of components depends on the

Table 1 Growth parameters favoring the ZB or WZ structure in typical III–V nanowires. All nanowires were grown by the VLS method except for those in ref. 43 grown by SA-MOCVD

		Parameters			
Structure	Material	*T*/°C	V/III ratio	Diameter/nm	Ref.
Wurtzite (WZ)	GaAs	550	42	—	18
	InAs	420–480	130	14–75	9,34
		500	2.9	60	27
	InP	430	8.26	—	18
		400–510	700	30	40
		480–510	44–110	30	40
		660	18	105	43
Zinc-blende (ZB)	GaAs	450	93	50	24,39
		350	42	—	18
		430	14.25	40	45
	InAs	420–480	130	75–137	9,34
		400	46	60	27
	InP	380	8.26	30	18
		400–450	44–110	30	40
		600	55	220	43

Table 2 Comparison of the bandgap and valence band splitting energies of common III–V materials in ZB and WZ phase

Material	InP	InSb	InAs	GaAs	GaSb	GaN
Zinc blende (Cubic)	Primary	Primary	Primary	Primary	Primary	Secondary (β-GaN)
E_g/eV @ 0 K	1.42[22,48–50]	0.24[45,51,52]	0.42[50,53,54]	1.52[50,52,55–57]	0.81–0.82[50,52,55]	3.3[50,52,58]
E_g/eV @ 300 K	1.34–1.35[53,55,59]	0.17–0.18[50,51,55,59]	0.35–0.36[50,53,59]	1.42–1.44[56,57,59]	0.72–0.75[50,52,55,59]	3.2[50,52,55,58]
$\Delta_{Spin–Orbit}$/meV	108[50]	810[50]	390[50]	341[50,52]	760[50]	17[50]
	114[52,b]	870[52]	430[52]		780[52,b]	16.3[52,b]
Wurtzite (Hexagonal)	Secondary	Secondary	Secondary	Secondary	Secondary	Primary (α-GaN)
E_g/eV @ 0 K	A - 1.47–1.50[22,48,49,60,61]	0.287[60]	0.47–0.48[60,62]	1.50–1.55[46,60,63–65]	0.509[60]	A- 3.48–3.51[50,66]
	B - 1.54[61]					B- 3.49[66]
	C - 1.67[61]					C- 3.51[66]
E_g/eV @ 300 K	1.43[48]	–[a]	–[a]	1.39[64]	–[a]	A- 3.4[50,66,67]
						B- 3.42[66]
						C- 3.46[66]
$\Delta_{Crystal}$/meV	82[65]	159[60]	195[60]	244[60]	239[60]	15.2[52,b]
	52[61]					9.8–19[50,55]
$\Delta_{Spin–Orbit}$/meV	108[50,60]	787[60]	379[60]	351[60]	777[60]	15.5[52,b]
						14–16.8[50,55]

[a] No data available to our knowledge. [b] Mean value over several references.

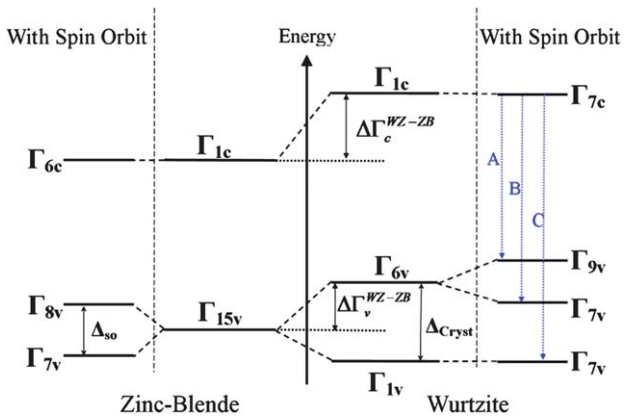

Fig. 2 Schematic of the band energies at the Γ point in WZ and ZB structures with and without the inclusion of spin–orbit interaction. The values of Δ_{SO} and Δ_{Cryst} for different materials are reported in Table 2. The transitions labeled A, B and C correspond to those in Table 2. Adapted from ref. 60, 68 & 69.

crystalline structure. Cubic structures (such as ZB) do not present anisotropy in optical transitions,[68,69] hence the tensor has only one component, whereas in hexagonal crystal structures (such as WZ) the tensor has two components that depend on the polarization state being either parallel ($E_{\parallel}z$) or orthogonal ($E_{\perp}z$) to the z axis. Consequently, the oscillator strength of a direct transition depends on the chosen orientation of the crystal. Moreover, in the case of nanowires, symmetry breaking leads unavoidably to the increase of the number of tensor components, thus at least two components ($E_{\parallel}z$ and $E_{\perp}z$, where z indicates the wire axis) are always present. The square values of the dipole matrix elements, which allow estimating the oscillator strength of direct transitions, have been calculated by the full-potential linearized augmented plane wave method[70] within the generalized gradient approximation[71] for the first direct transition in the Γ point, namely Γ_{1c}–Γ_{15v} in the ZB and Γ_{1c}–Γ_{6v} in the WZ structure. The results for some III–V compounds are presented in Table 3. In these calculations the spin–orbit interaction was neglected. Because of the sizable underestimation of bandgap energies typical of the generalized gradient approximation, in the case of GaSb in the WZ phase the bandgap in the Γ point vanished and calculation of the corresponding dipole matrix element was not possible.

The calculations clearly show that in the WZ phase, the values of the oscillator strength of the Γ_{1c}–Γ_{6v} transition differ by orders of magnitude for $E_{\parallel}z$ and $E_{\perp}z$ light polarization, in agreement with the strong anisotropy expected from symmetry considerations and previous predictions.[68,69,72] Moreover, the strength of the Γ_{1c}–Γ_{6v} transition with electric field orthogonal to the z axis is comparable to the Γ_{1c}–Γ_{15v} transition in the ZB structure for all materials considered. The Γ_{1c}–Γ_{1v} transition in the WZ phase is expected to be polarized parallel to the z direction,[68,69,72] however our computation code did not allow quantitative evaluation of its oscillator strength.

Slightly different band symmetries and polarization selection rules for the transitions are expected when considering spin–orbit interaction. Under the effect of spin–orbit coupling Δ_{SO} (see Table 2), the Γ_{6v} valence band in WZ splits into a higher (Γ_{9v}) and a lower (Γ_{7v}) energy band. Consequently, the Γ_{7c}–Γ_{9v} transition (labeled A in Fig. 2) maintains the same orthogonal selection rule as the Γ_{1c}–Γ_{6v} transition in the absence of spin–orbit interaction. The second and third higher valence bands have the same Γ_7 symmetry as the conduction band, thus two additional Γ_{7c}–Γ_{7v} transitions (labeled B and C in Fig. 2) appear. These transitions, however, do not exhibit any preferential polarization. In the case of GaAs nanowires the symmetry of the lowest conduction band is still controversial. Theoretical works have demonstrated that both Γ_7 or Γ_8 symmetries exist,[60,65] while recent micro Raman measurements attribute a Γ_7 symmetry to this band.[64,73] In general, under the quasicubic approximation, the differences in energy between the valence bands induced by spin–orbit interaction in the WZ structure are given by:[74]

$$E\left(\Gamma_{7v}^{1,2}\right) - E(\Gamma_{9v}) = -\frac{\Delta_{SO}+\Delta_{Cryst}}{2} \pm \frac{\sqrt{\left(\Delta_{SO}+\Delta_{Cryst}\right)^2 - \frac{8}{3}\Delta_{SO}\Delta_{Cryst}}}{2} \quad (1)$$

Similarly, the Γ_{15v} valence band of the ZB structure splits into a higher (Γ_{8v}) and a lower (Γ_{7v}) energy band, therefore two

Table 3 Calculated square values of dipole matrix elements for the lowest energy transition in ZB and WZ structure for different III–V materials (without considering spin–orbit). The last column indicates the preferred polarization of a given transition

Structure	Transition	InP	GaN	GaAs	GaSb	Polarization selection rule[68,69]
ZB	Γ_{1c}–Γ_{15v}	7.4×10^{-2}	6.2×10^{-2}	0.10	0.11	All polarizations allowed
WZ	Γ_{1c}–Γ_{6v} ($E_{\perp}z$)	0.10	9.0×10^{-2}	0.13	—[a]	Allowed
	Γ_{1c}–Γ_{6v} ($E_{\parallel}z$)	1.1×10^{-17}	1.6×10^{-16}	8.5×10^{-17}	—[a]	Forbidden

[a] Values could not be obtained.

transitions (Γ_{6c}–Γ_{8v} and Γ_{6c}–Γ_{7v}) are possible. However, even by considering spin–orbit interaction, these transitions remain unpolarized.[68,69]

From these general considerations it is apparent that detailed knowledge of the correlation between structure and dipole selection rules (and their polarization anisotropy) is a fundamental step in unraveling the *intrinsic* emission and absorption properties of nanowire crystals. The following Section will focus on additional complications introduced by *extrinsic* effects related to refractive index mismatch in high aspect ratio structures.

4. Anisotropic optical properties of III–V nanowires

4.1. Refractive index mismatch

The high aspect ratio of III–V nanowires combined with a large refractive index contrast with the surrounding environment induce strong polarization anisotropy of the absorbed and emitted radiation. Polarized optical absorption and emission of individual III–V nanowires have first been observed by Wang *et al.* in photoluminescence and photoconductivity measurements of individual InP nanowires.[75] The large polarization anisotropy of the absorption is typically manifested in the strong dependence of photoluminescence intensity and photoconductance of single nanowires on the polarization of the excitation beam relative to the nanowire axis. Similarly, for a fixed polarization of the excitation, the polarization of the emission is strongly anisotropic and photoluminescence intensity depends on the angular orientation of the analyzer. This was observed in both individual (GaAs, GaN) nanowires[76,77] and (InP) nanowire ensembles.[78]

Theoretical electromagnetic modeling conducted by Ruda *et al.* highlighted the importance of the dielectric constant mismatch between freestanding nanowires (with dielectric constant ε) and their surrounding media (with dielectric constant ε_0) to their absorption and emission properties.[79,80] The absorption (emission) anisotropy is generally defined as the ratio between absorbed (emitted) light intensity with polarization parallel ($I_{\parallel}$) and orthogonal ($I_{\perp}$) to the nanowire axis. In the case of absorption, $I_{\parallel}$ and $I_{\perp}$ can be evaluated by calculating the electric field inside an infinitely long cylindrical nanowire illuminated by an incident plane wave. Ruda *et al.* have shown that, for a nanowire with considerably smaller diameter than the incident wavelength (typically smaller than 20 nm), light polarized in the parallel direction is absorbed more effectively than light with perpendicular polarization, and the absorption anisotropy depends exclusively on the ratio $\varepsilon/\varepsilon_0$.[79] This result is obtained in the case of a thin nanowire where the continuity of the tangential component of the electrical field at the boundary with the sidewalls imposes that $E_{\parallel \mathrm{in}} = E_{\parallel \mathrm{out}}$ (where E_{in} and E_{out} are the electric field inside and outside the wire, respectively), but the perpendicular component of the electric field is attenuated inside the wire leading to the relationship:

$$E_{\perp \mathrm{in}} = \frac{2\varepsilon_0}{\varepsilon + \varepsilon_0} E_{\perp \mathrm{out}} \tag{2}$$

However, the previous formalism is no longer valid for nanowires with larger diameter since the inner electric field can no longer be considered uniform. Indeed, as the diameter increases, the distribution of the electric field becomes more complex due to the coexistence of guided modes with different spatial profiles. Notably, the appearance of transverse guided modes with large transverse electric field amplitude reduces the absorption anisotropy.[80–82]

For emission, Ruda *et al.* have also showed that the emitting dipole moment of the entire nanowire $d_0 = (d_{0x}, d_{0y}, d_{0z})$ can be modeled by an effective emitting dipole moment $d = (d_x, d_y = d_x, d_z)$ with the following components:[80]

$$d_x = d_{0x}\sqrt{\varepsilon} \times \frac{J_1'(ka)H_1^{(1)}(ka) - J_1(ka)H_1^{(1)'}(ka)}{\sqrt{\varepsilon_0} * J_1'(ka)H_1^{(1)}(k_0a) - \sqrt{\varepsilon} * J_1(ka)H_1^{(1)'}(k_0a)} \tag{3}$$

$$d_z = d_{0z}\sqrt{\varepsilon} \times \frac{J_1(ka)H_0^{(1)}(ka) - J_0(ka)H_1^{(1)}(ka)}{\sqrt{\varepsilon} * J_1(ka)H_0^{(1)}(k_0a) - \sqrt{\varepsilon_0} * J_0(ka)H_1^{(1)}(k_0a)} \tag{4}$$

where a denotes the nanowire radius, and $k = \sqrt{\varepsilon}*\omega/c$ and $k_0 = \sqrt{\varepsilon_0}*\omega/c$ are the wavevectors in the dielectric (nanowire) and air, respectively. J_m ($H^{(1)}{}_m$) stands for the Bessel (Hankel) function of the first kind, and the primes denote their first derivative with respect to the argument. The ratio of emitted light intensity in the two polarizations is then described by:

$$\frac{I_{\parallel}^{e}}{I_{\perp}^{e}} = \frac{d_x^2 + 2d_z^2}{3d_x^2} \tag{5}$$

Fig. 3 shows the dependence of the emission anisotropy derived from eqn (3)–(5) as a function of nanowire radius in common III–V materials (the curves were calculated at energies below bandgap and using the dielectric constants from ref. 83). In the case of very thin nanowires (with diameter smaller than 20 nm) the emission with parallel polarization is predominant and eqn (5) tends to the static value:[79]

$$\frac{I_{\parallel}^{e}}{I_{\perp}^{e}} = \frac{(\varepsilon + \varepsilon_0)^2 + 2\varepsilon_0^2}{6\varepsilon_0^2} \tag{6}$$

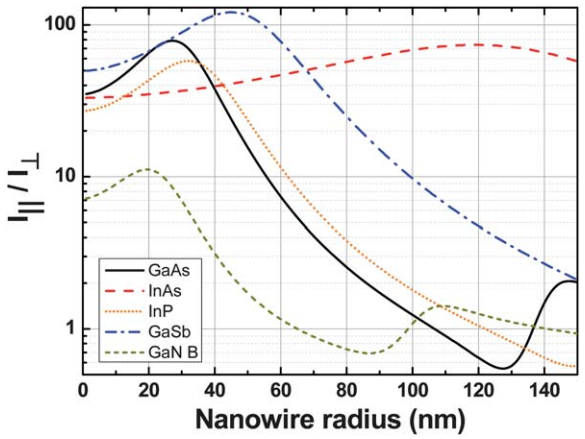

Fig. 3 Polarization anisotropy of the emitted light *versus* the radius of the nanowire for different III–V materials.

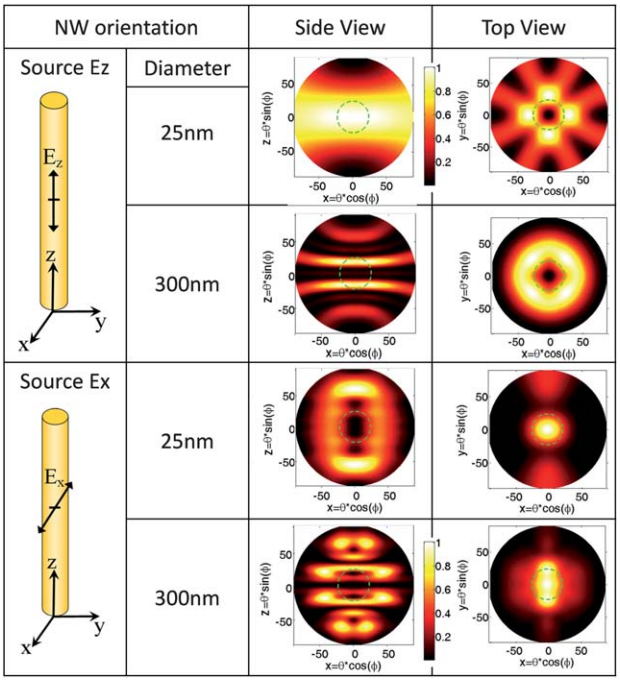

Fig. 4 Top and side views of the far-field radiation patterns from a freestanding GaAs nanowire obtained with excitation polarized parallel and perpendicular to the nanowire *z*-axis and for different nanowire diameters. The dashed green circle represents the ideal collection angle of an objective with numerical aperture of 0.4.

For small diameters, only the HE_{11} mode of the cylindrical waveguide can exist due to the absence of a cut-off frequency.[81,82] However, for larger diameters, guided modes start playing a major role in determining the emission polarization, similar to the case of absorption. Upon reaching the cut-off radius of the first transverse TE_{01} mode (for instance, above $r = 110$ nm in GaAs), the total electric field inside the wire is primarily oriented perpendicularly to the wire axis, hence forces the emission polarization in the perpendicular direction.[77,84] At even larger diameters, TM_{01} and additional hybrid modes intermix and the resulting polarization returns parallel to the nanowire axis.

In actual photoluminescence experiments, the measured light intensity further depends on the numerical aperture of the collection setup and on the distribution of the emitted radiation in the far-field. Therefore, to properly evaluate the anisotropy, one must consider the far-field radiation pattern. The details of the angular distribution of guided and free space modes of a vertical nanowire have been previously given by Maslov *et al.*[82,85,86] However, the overall radiation pattern in the far-field depends also on additional parameters such as the position and the polarization of the source, and the diameter of the nanowire. Thus three dimensional Finite Difference Time Domain (3D-FDTD) simulations of the far-field distribution of the emitted intensity in freestanding GaAs nanowire have been conducted to draw a more realistic picture. Fig. 4 shows the results for the two extreme cases of small (25 nm) and large (300 nm) diameter nanowires. For near-field calculations,[87] the emitting source was a single dipole placed at the center of the 3μm long nanowire and was modeled by a continuous current source emitting at a fixed wavelength of 870 nm. The polarization of the source was fixed either in the parallel (E_z) or in the perpendicular (E_x) direction with respect to the nanowire axis to illustrate the effect of the source polarization on the angular distribution of the radiation. The far-field patterns were obtained using the approach outlined in ref. 85, 88 & 89. The intensities in Fig. 4 are normalised with respect to the maximum of each pattern.

For small diameter nanowires the far-field patterns in Fig. 4 exhibit lateral emission in the case of parallel excitation, while emission is collinear to the nanowire axis when the source has perpendicular polarization.[82,85] For larger diameters, the appearance of higher-order guided modes may shape the longitudinal profile of the emission. In the particular case considered here of a 300 nm GaAs nanowire, the far-field radiation patterns calculated with parallel and perpendicular sources are fairly similar, except for the appearance of collinear emission lobes in the case of perpendicular excitation.

Given the strong spatial anisotropy of the radiation patterns, the light intensity collected from the nanowire is strongly dependent on the measuring configuration and the collection angles. Optical properties of individual nanowires are usually measured with nanowires lying horizontally on a host substrate and collection normal to it. This configuration corresponds to the side-view panels in Fig. 4. For intrinsically isotropic systems (*e.g.* ZB structures) or unpolarized excitation, the resulting distribution of the emission would then result from the superposition of the radiation patterns obtained for the two polarizations of the source, whereas for anisotropic systems (*e.g.* WZ structures) or selectively polarized excitation the far-field radiation pattern can be tuned between the two configurations of the source polarization. For a given radiation pattern, the emission anisotropy in eqn (5) and Fig. 3 determines the relative intensity of the two polarizations. The experimental observation of the optical anisotropy of III–V nanowires is discussed in the following Section in view of the interplay between intrinsic crystalline properties, dielectric effects, and measuring configuration.

4.2. Experimental observation of optical anisotropy

Direct observation of the correlation between crystalline structure and polarization anisotropy in III–V nanowires was first reported by Mishra *et al.*[48] Low-temperature photoluminescence measurements of individual InP nanowires crystallized in either of the two phases have shown strongly polarized emission with opposite polarizations upon excitation with circularly polarized light (Fig. 5a). While nanowires with ZB structure were found to emit preferentially with parallel polarization, WZ nanowires showed stronger emission intensity with perpendicular polarization. As mentioned previously, the parallel polarized emission in otherwise isotropic ZB structure is induced by the dielectric effects in high aspect-ratio nanowires. In the case of WZ, the polarization selection rules summarized in Table 3 are mainly responsible for the orthogonally polarized emission. Moreover, in this case dielectric effects due to the refractive index mismatch (favoring parallel emission) and the intrinsic anisotropy due to the crystalline structure (favoring perpendicular emission) have opposite trends and compete with each other. Interestingly, a clear manifestation of the effect of refractive index mismatch can be seen at zero polarization angle, where the emission does not vanish despite of the polarization selection rules. The low-temperature photoluminescence spectra of three different nanowires with single crystal structure (either pure ZB or WZ) have shown a clear shift in emission energy between the two phases (Fig. 5b), in agreement with the bandgap energies predicted by *ab initio* calculations (Table 2).

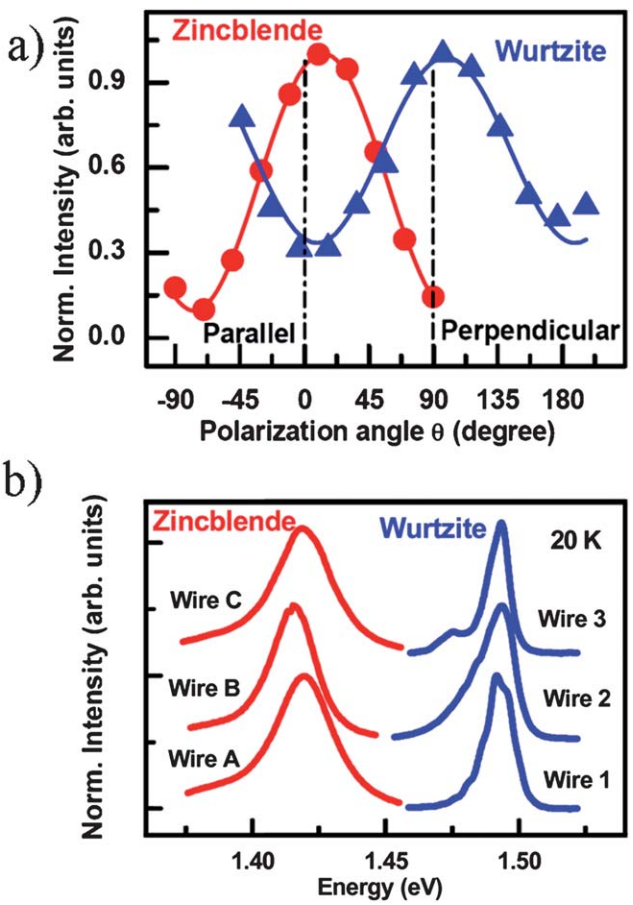

Fig. 5 Low-temperature ($T = 15$ K) photoluminescence of single InP nanowires with pure ZB and WZ structure. (a) Polarized photoluminescence. (b) Emission spectra. Reprinted with permission from ref. 48 (copyright 2007, American Institute of Physics).

When grown side by side, ZB and WZ phases form a polytypic junction with the energetic shown in Fig. 2, where the energy difference between the lowest conduction bands and the highest valence bands is denoted by $\Delta\Gamma_c^{WZ-ZB}$ and $\Delta\Gamma_v^{WZ-ZB}$, respectively. Murayama *et al.* have found that both these differences are positive in various III–V semiconductors, indicating a type-II band alignment (Table 4).[65]

As outlined in Section 2, it is possible to induce ZB/WZ polytypism by controlling the nanowire growth parameters, hence to promote the formation of type-II heterojunctions between segments in the ZB and WZ phase within a single material system.[9,90–95] When stacks of alternating segments with WZ and ZB phases are formed along the nanowire axis, discreet energy levels appear in the lowest conduction band and in the highest valence band due to the creation of multiple quantum wells. Holes will then tend to be confined in sections with predominance of WZ phase, while electrons to aggregate in ZB dominant segments.[23,49,93,96] As a result, optical transitions may occur between the lowest conduction band of the ZB phase and the highest valence band of the WZ phase, and different emission energies may then be obtained depending on the length and the periodicity of the stacking fault.[23,63] Fig. 6 shows cathodoluminescence images of a GaAs nanowire with predominant ZB structure and a varying percentage of WZ phase along its axis.[23] While the primary ZB structure displays the expected emission at 1.51 eV, additional emission energies are observed at different positions along the nanowire due to different concentrations of WZ phase and the different widths of the wells. As a result, the overall absorption and emission spectra of the nanowire are broadened by the presence of stacked quantum wells, which may be useful in some light harvesting or lightning applications.[49,63] Furthermore, the *periodic* alternation of WZ and ZB phases along the nanowire axis has been proposed to realize polytypic superlattices.[9]

Recently, there has been considerable interest in III–V nanowire twinning superlattices, where the spontaneous occurrence of twin defects introduces a periodic spatial modulation of the primary ZB phase (see Section 2). Mini-bands and the opening of zero energy gaps at the superlattice Brillouin zone boundary have been predicted in such structures, but the resulting optical properties and dipole selection rules are yet to be defined.[97]

Table 4 Energy difference between the valence and conduction bands in ZB and WZ III–V semiconductors at $T = 0$ K. The values are extracted from ref. 65

Material	InP	InSb	InAs	GaAs	GaSb	GaN
$\Delta\Gamma_v^{WZ-ZB}$/meV	45	57	46	84	89	34
$\Delta\Gamma_c^{WZ-ZB}$/meV	129	86	86	117	102	154

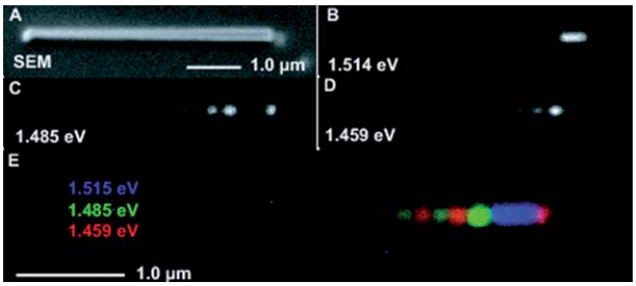

Fig. 6 Cathodoluminescence of a heterostructured GaAs nanowire. (a) SEM image of a composite ZB nanowire with 30 ± 10% WZ phase. (b–d) Cathodoluminescence images recorded for different emission energies. (e) Composite cathodoluminescence image. Reprinted with permission from ref. 23 (copyright 2009 by the American Physical Society).

5. Conclusion and perspectives

Although extensively studied in the past few years, the fundamental phenomena leading to the optical and spatial anisotropy of the absorption and emission properties of quasi-one dimensional systems, particularly III–V nanowires, are a research topic of ongoing interest from both fundamental and applied perspective. An overview of the *intrinsic* and *extrinsic* effects known from the literature to determine the strong anisotropy of optical absorption and emission is presented, together with a general workflow that points to the understanding of the detailed crystalline structure, dielectric effects of specific materials, and the spatial light distribution in the far-field is outlined to facilitate future comparisons between experimental observations and theoretical expectations. It is shown how current advances in controlled growth of bottom-up III–V nanowires enable the synthesis of nanowire heterostructures of increasingly greater complexity and abruptness (*e.g.* single polytypic junctions, stacks of polytypic quantum wells, and twinning superlattices) and the realization of optical experiments of increasingly higher accuracy and predictability (*e.g.* FDTD modeling, polarized micro-photoluminescence and cathodoluminescence), opening up new windows on the fundamental interaction of light with low-dimensional systems. The strong optical anisotropy should be accounted in proposed applications of III–V nanowires, and conversely could be exploited in emerging optoelectronic devices such as polarization memory devices,[78,79] polarization sensitive photodetectors,[1] or polarized light-emitting diodes.[98] A bright future lies ahead for III–V nanowire photonics.

Acknowledgements

C. W. gratefully acknowledges the joint-PhD program between the Nanyang Technological University and ParisTech. The authors are grateful to Ms. G. Vest for her help in reviewing some articles and for the useful discussions about FDTD simulations, and Dr A. De Rossi, Dr S. Combrie, and Dr N. V. Q. Tran for their help in developing the code for the calculation of far-field patterns. This work was financially supported by the NTU NAP startup grant M58110065, the MERLION Programme 2010 of the French Embassy in Singapore (dossier 2.04.10), and the Funding of Initiatives in Support of NTU 2015 (M58110092). D.M. acknowledges the partial financial support from the Belarusian government program of scientific research (Grant 2.4.16).

Notes and References

1 C. Soci, A. Zhang, X. Y. Bao, H. Kim, Y. Lo and D. L. Wang, *J. Nanosci. Nanotechnol.*, 2010, **10**, 1430–1449.
2 K. Tomioka, T. Tanaka, S. Hara, K. Hiruma and T. Fukui, *IEEE J. Sel. Top. Quantum Electron.*, 2011, **17**, 1112.
3 Z. Fan, H. Razavi, J.-w. Do, A. Moriwaki, O. Ergen, Y.-L. Chueh, P. W. Leu, J. C. Ho, T. Takahashi, L. A. Reichertz, S. Neale, K. Yu, M. Wu, J. W. Ager and A. Javey, *Nat. Mater.*, 2009, **8**, 648–653.
4 J. Motohisa, J. Noborisaka, J. Takeda, M. Inari and T. Fukui, *J. Cryst. Growth*, 2004, **272**, 180–185.
5 D. Dalacu, A. Kam, D. Guy Austing, X. Wu, J. Lapointe, G. C. Aers and P. J. Poole, *Nanotechnology*, 2009, **20**, 395602.
6 R. E. Algra, M. A. Verheijen, M. T. Borgström, L.-F. Feiner, G. Immink, W. J. P. van Enckevort, E. Vlieg and E. P. A. M. Bakkers, *Nature*, 2008, **456**, 369–372.
7 R. E. Algra, M. A. Verheijen, L.-F. Feiner, G. G. W. Immink, W. J. P. v. Enckevort, E. Vlieg and E. P. A. M. Bakkers, *Nano Lett.*, 2011, **11**, 1259–1264.
8 Q. Xiong, J. Wang and P. C. Eklund, *Nano Lett.*, 2006, **6**, 2736–2742.
9 P. Caroff, K. A. Dick, J. Johansson, M. E. Messing, K. Deppert and L. Samuelson, *Nat. Nanotechnol.*, 2008, **4**, 50–55.
10 S. A. Dayeh, D. P. R. Aplin, X. Zhou, P. K. L. Yu, E. T. Yu and D. Wang, *Small*, 2007, **3**, 326–332.
11 J. W. W. Van Tilburg, R. E. Algra, W. G. G. Immink, M. Verheijen, E. P. A. M. Bakkers and L. P. Kouwenhoven, *Semicond. Sci. Technol.*, 2010, **25**, 024011.
12 S. A. Dayeh, C. Soci, X.-Y. Bao and D. Wang, *Nano Today*, 2009, **4**, 347–358.
13 S. Gradecak, F. Qian, Y. Li, H. G. Park and C. M. Lieber, *Appl. Phys. Lett.*, 2005, **87**, 173111.
14 H. Kind, H. Q. Yan, B. Messer, M. Law and P. D. Yang, *Adv. Mater.*, 2002, **14**, 158.
15 S. Jin, D. M. Whang, M. C. McAlpine, R. S. Friedman, Y. Wu and C. M. Lieber, *Nano Lett.*, 2004, **4**, 915–919.
16 K. A. Dick, K. Deppert, L. S. Karlsson, W. Seifert, L. R. Wallenberg and L. Samuelson, *Nano Lett.*, 2006, **6**, 2842–2847.
17 J. Claudon, J. Bleuse, N. S. Malik, M. Bazin, P. Jaffrennou, N. Gregersen, C. Sauvan, P. Lalanne and J.-M. Gerard, *Nat. Photonics*, 2010, **4**, 174–177.
18 K. A. Dick, P. Caroff, J. Bolinsson, M. E. Messing, J. Johansson, K. Deppert, L. R. Wallenberg and L. Samuelson, *Semicond. Sci. Technol.*, 2010, **25**, 024009.
19 S. A. Dayeh, *Semicond. Sci. Technol.*, 2010, **25**, 024004.
20 M. Koguchi, H. Kakibayashi, M. Yazawa, K. Hiruma and T. Katsuyama, *Jpn. J. Appl. Phys.*, 1992, **31**, 2061–2065.
21 K. Tomioka, J. Motohisa, S. Hara and T. Fukui, *Jpn. J. Appl. Phys.*, 2007, **46**, L1102–L1104.
22 K. Ikejiri, Y. Kitauchi, K. Tomioka, J. Motohisa and T. Fukui, *Nano Lett.*, 2011, **11**, 4314–4318.
23 D. Spirkoska, J. Arbiol, A. Gustafsson, S. Conesa-Boj, F. Glas, I. Zardo, M. Heigoldt, M. H. Gass, A. L. Bleloch, S. Estrade, M. Kaniber, J. Rossler, F. Peiro, J. R. Morante, G. Abstreiter, L. Samuelson and A. F. I. Morral, *Phys. Rev. B: Condens. Matter Mater. Phys.*, 2009, **80**, 245325.
24 H. J. Joyce, Q. Gao, H. H. Tan, C. Jagadish, Y. Kim, M. A. Fickenscher, S. Perera, T. B. Hoang, L. M. Smith, H. E. Jackson, J. M. Yarrison-Rice, X. Zhang and J. Zou, *Adv. Funct. Mater.*, 2008, **18**, 3794–3800.
25 S. Paiman, Q. Gao, H. H. Tan, C. Jagadish, K. Pemasiri, M. Montazeri, H. E. Jackson, L. M. Smith, J. M. Yarrison-Rice, X. Zhang and J. Zou, *Nanotechnology*, 2009, **20**, 225606.
26 C. Soci, X.-Y. Bao, D. P. R. Aplin and D. Wang, *Nano Lett.*, 2008, **8**, 4275–4282.
27 H. J. Joyce, J. Wong-Leung, Q. Gao, H. H. Tan and C. Jagadish, *Nano Lett.*, 2010, **10**, 908–915.
28 A. I. Persson, B. J. Ohlsson, S. Jeppesen and L. Samuelson, *J. Cryst. Growth*, 2004, **272**, 167–174.
29 R. S. Wagner and W. C. Ellis, *Appl. Phys. Lett.*, 1964, **4**, 89–90.

30 J. Johansson, L. S. Karlsson, C. Patrik, T. Svensson, T. Mårtensson, B. A. Wacaser, K. Deppert, L. Samuelson and W. Seifert, *Nat. Mater.*, 2006, **5**, 574–580.
31 F. Glas, J.-C. Harmand and G. Patriarche, *Phys. Rev. Lett.*, 2007, **99**, 146101.
32 V. Dubrovskii, N. Sibirev, G. Cirlin, J. Harmand and V. Ustinov, *Phys. Rev. E: Stat., Nonlinear, Soft Matter Phys.*, 2006, **73**, 021603.
33 T. Akiyama, K. Sano, K. Nakamura and T. Ito, *Jpn. J. Appl. Phys.*, 2006, **45**, L275–L278.
34 J. Johansson, K. A. Dick, P. Caroff, M. E. Messing, J. Bolinsson, K. Deppert and L. Samuelson, *J. Phys. Chem. C*, 2010, **114**, 3837–3842.
35 V. G. Dubrovskii and N. V. Sibirev, *Phys. Rev. B: Condens. Matter Mater. Phys.*, 2008, **77**, 035414.
36 V. G. Dubrovskii, N. V. Sibirev, J. C. Harmand and F. Glas, *Phys. Rev. B: Condens. Matter Mater. Phys.*, 2008, **78**, 235301.
37 F. Glas, G. Patriarche and J. C. Harmand, *J. Phys.: Conf. Ser.*, 2010, **209**, 012002.
38 H. J. Joyce, Q. Gao, H. H. Tan, C. Jagadish, Y. Kim, M. A. Fickenscher, S. Perera, T. B. Hoang, L. M. Smith, H. E. Jackson, J. M. Yarrison-Rice, X. Zhang and J. Zou, *Nano Lett.*, 2009, **9**, 695–701.
39 H. J. Joyce, Q. Gao, H. Hoe Tan, C. Jagadish, Y. Kim, J. Zou, L. M. Smith, H. E. Jackson, J. M. Yarrison-Rice, P. Parkinson and M. B. Johnston, *Prog. Quantum Electron.*, 2011, **35**, 23–75.
40 S. Paiman, Q. Gao, H. J. Joyce, Y. Kim, H. H. Tan, C. Jagadish, X. Zhang, Y. Guo and J. Zou, *J. Phys. D: Appl. Phys.*, 2010, **43**, 445402.
41 X.-Y. Bao, C. Soci, D. Susac, J. Bratvold, D. P. R. Aplin, W. Wei, C.-Y. Chen, S. A. Dayeh, K. L. Kavanagh and D. Wang, *Nano Lett.*, 2008, **8**, 3755–3760.
42 I. Soshnikov, G. Cirlin, A. Tonkikh, V. Nevedomskiĭ, Y. Samsonenko and V. Ustinov, *Phys. Solid State*, 2007, **49**, 1440–1445.
43 Y. Kitauchi, Y. Kobayashi, K. Tomioka, S. Hara, K. Hiruma, T. Fukui and J. Motohisa, *Nano Lett.*, 2010, **10**, 1699–1703.
44 R. E. Algra, M. A. Verheijen, L.-F. Feiner, G. G. W. Immink, R. Theissmann, W. J. P. v. Enckevort, E. Vlieg and E. P. A. M. Bakkers, *Nano Lett.*, 2010, **10**, 2349–2356.
45 X. Dai, S. A. Dayeh and C. Soci, unpublished work.
46 T. B. Hoang, *Appl. Phys. Lett.*, 2009, **94**, 133105.
47 L. P. Bouckaert, R. Smoluchowski and E. Wigner, *Phys. Rev.*, 1936, **50**, 58–67.
48 A. Mishra, L. V. Titova, T. B. Hoang, H. E. Jackson, L. M. Smith, J. M. Yarrison-Rice, Y. Kim, H. J. Joyce, Q. Gao, H. H. Tan and C. Jagadish, *Appl. Phys. Lett.*, 2007, **91**, 263104.
49 J. M. Bao, D. C. Bell, F. Capasso, J. B. Wagner, T. Martensson, J. Tragardh and L. Samuelson, *Nano Lett.*, 2008, **8**, 836–841.
50 I. Vurgaftman, J. R. Meyer and L. R. Ram-Mohan, *J. Appl. Phys.*, 2001, **89**, 5815–5875.
51 C. Littler, *Appl. Phys. Lett.*, 1985, **46**, 986.
52 S. Adachi, *Handbook on physical properties of semiconductors*, Kluwer Academic Publishers, 2004.
53 Y. P. Varshni, *Physica*, 1967, **34**, 149.
54 Z. Fang, K. Ma, D. Jaw, R. Cohen and G. Stringfellow, *J. Appl. Phys.*, 1990, **67**, 7034.
55 O. Madelung, *Semiconductors: data handbook*, Springer, 2004.
56 J. S. Blakemore, *J. Appl. Phys.*, 1982, **53**, R123–R181.
57 M. B. Panish and H. C. Casey, *J. Appl. Phys.*, 1969, **40**, 163.
58 R. S. L. M. E. Levinshtein, M. S. Shur, *Properties of Advanced Semiconductor Materials, GaN, AlN, InN, BN, SiC, SiGe*, John Wiley & Sons, New-York, 2001.
59 S. Adachi, *J. Appl. Phys.*, 1989, **66**, 6030–6040.
60 A. De and C. E. Pryor, *Phys. Rev. B: Condens. Matter Mater. Phys.*, 2010, **81**, 155210.
61 S. Perera, K. Pemasiri, M. A. Fickenscher, H. E. Jackson, L. M. Smith, J. Yarrison-Rice, S. Paiman, Q. Gao, H. H. Tan and C. Jagadish, *Appl. Phys. Lett.*, 2010, **97**, 023106.
62 Z. Zanolli, F. Fuchs, J. Furthmueller, U. von Barth and F. Bechstedt, *Phys. Rev. B: Condens. Matter Mater. Phys.*, 2007, **75**, 245121.
63 M. Heiss, S. Conesa-Boj, J. Ren, H. H. Tseng, A. Gali, A. Rudolph, E. Uccelli, F. Peiro, J. R. Morante, D. Schuh, E. Reiger, E. Kaxiras, J. Arbiol and A. F. I. Morral, *Phys. Rev. B: Condens. Matter Mater. Phys.*, 2011, **83**, 045303.
64 B. Ketterer, M. Heiss, M. J. Livrozet, A. Rudolph, E. Reiger and A. Fontcuberta i Morral, *Phys. Rev. B: Condens. Matter Mater. Phys.*, 2011, **83**, 125307.
65 M. Murayama and T. Nakayama, *Phys. Rev. B: Condens. Matter*, 1994, **49**, 4710–4724.
66 C. F. Li, Y. S. Huang, L. Malikova and F. H. Pollak, *Phys. Rev. B: Condens. Matter*, 1997, **55**, 9251.
67 H. G. Yu, *Chem. Phys. Lett.*, 2011, **512**, 231–236.
68 J. L. Birman, *Phys. Rev.*, 1959, **114**, 1490–1492.
69 J. L. Birman, *Phys. Rev. Lett.*, 1959, **2**, 157–159.
70 K. S. P. Blaha, G. K. H. Madsen, D. Kvasnicka and J. Luitz, WIEN2k; An augmented Plane Wave + Local Orbitals Program for Calculating Crystal Properties, 2001.
71 J. P. Perdew, K. Burke and M. Ernzerhof, *Phys. Rev. Lett.*, 1996, **77**, 3865–3868.
72 P. Tronc, Y. E. Kitaev, G. Wang, M. F. Limonov, A. G. Panfilov and G. Neu, *Phys. Status Solidi B*, 1999, **216**, 599–603.
73 B. Ketterer, M. Heiss, E. Uccelli, J. Arbiol and A. Fontcuberta i Morral, *ACS Nano*, 2011, **5**, 7585–7592.
74 S. L. Chuang and C. S. Chang, *Phys. Rev. B: Condens. Matter*, 1996, **54**, 2491–2504.
75 J. F. Wang, M. S. Gudiksen, X. F. Duan, Y. Cui and C. M. Lieber, *Science*, 2001, **293**, 1455–1457.
76 G. Zhang, K. Tateno, H. Sanada, T. Tawara, H. Gotoh and H. Nakano, *Appl. Phys. Lett.*, 2009, **95**, 123104.
77 H.-Y. Chen, Y.-C. Yang, H.-W. Lin, S.-C. Chang and S. Gwo, *Opt. Express*, 2008, **16**, 13465–13475.
78 L. Fang, X. Zhao, Y.-H. Chiu, D. Ko, K. M. Reddy, T. R. Lemberger, N. P. Padture, F. Yang and E. Johnston-Halperin, *Appl. Phys. Lett.*, 2011, **99**, 141101–141103.
79 H. E. Ruda and A. Shik, *Phys. Rev. B: Condens. Matter Mater. Phys.*, 2005, **72**, 115308.
80 H. E. Ruda and A. Shik, *J. Appl. Phys.*, 2006, **100**, 024314.
81 A.-L. Henneghien, B. Gayral, Y. Désières and J.-M. Gérard, *J. Opt. Soc. Am. B*, 2009, **26**, 2396–2403.
82 A. V. Maslov and C. Z. Ning, *Modal properties of semiconductor nanowires for laser applications*, San Jose, CA, USA, 2004.
83 S. Adachi, *Optical constants of crystalline and amorphous semiconductors: numerical data and graphical information*, Kluwer Academic Publishers, 1999.
84 A. V. Maslov and C. Z. Ning, *IEEE J. Quantum Electron.*, 2004, **40**, 1389–1397.
85 A. V. Maslov and C. Z. Ning, *Opt. Lett.*, 2004, **29**, 572–574.
86 A. V. Maslov, M. I. Bakunov and C. Z. Ning, *J. Appl. Phys.*, 2006, **99**, 024314–024310.
87 A. F. Oskooi, D. Roundy, M. Ibanescu, P. Bermel, J. D. Joannopoulos and S. G. Johnson, *Comput. Phys. Commun.*, 2010, **181**, 687–702.
88 J. Vuckovic, M. Loncar, H. Mabuchi and A. Scherer, *IEEE J. Quantum Electron.*, 2002, **38**, 850–856.
89 N.-V.-Q. Tran, S. Combrie, P. Colman, A. De Rossi and T. Mei, *Phys. Rev. B: Condens. Matter Mater. Phys.*, 2010, **82**, 075120.
90 N. Akopian, G. Patriarche, L. Liu, J. C. Harmand and V. Zwiller, *Nano Lett.*, 2010, **10**, 1198–1201.
91 K. A. Dick, C. Thelander, L. Samuelson and P. Caroff, *Nano Lett.*, 2010, **10**, 3494–3499.
92 P. Caroff, J. Bolinsson and J. Johansson, *IEEE J. Sel. Top. Quantum Electron.*, 2011, **17**, 829–846.
93 K. Pemasiri, M. Montazeri, R. Gass, L. M. Smith, H. E. Jackson, J. Yarrison-Rice, S. Paiman, Q. Gao, H. H. Tan, C. Jagadish, X. Zhang and J. Zou, *Nano Lett.*, 2009, **9**, 648–654.
94 J.-M. Jancu, K. Gauthron, L. Largeau, G. Patriarche, J.-C. Harmand and P. Voisin, *Appl. Phys. Lett.*, 2010, **97**, 041910.
95 A. F. Morral, *IEEE J. Sel. Top. Quantum Electron.*, 2011, **17**, 819–828.
96 T. B. Hoang, A. F. Moses, L. Ahtapodov, H. Zhou, D. L. Dheeraj, A. T. J. van Helvoort, B. O. Fimland and H. Weman, *Nano Lett.*, 2010, **10**, 2927–2933.
97 Z. Ikonić, G. P. Srivastava and J. C. Inkson, *Phys. Rev. B: Condens. Matter*, 1993, **48**, 17181–17193.
98 K. Tomioka, J. Motohisa, S. Hara, K. Hiruma and T. Fukui, *Nano Lett.*, 2010, **10**, 1639–1644.

